15.1 RADAR OBSERVATIONS OF VORTEX-RING ENTRAINMENT PATTERNS IN CUMULUS CLOUDS

Yonggang Wang* and Bart Geerts
University of Wyoming

1. INTRODUCTION

The representation of cumulus clouds in weather or climate models is challenging since they occur in a broad range of vertical and horizontal scales (e.g., Lopez 1977; Wielicki and Welch 1986), and the circulations generally are sub-gridscale (e.g., Khairoutdinov et al. 2008). Thus a number of Cu parameterizations have been developed to represent the effect of sub-gridscale convection on precipitation and the vertical profile of resolved variables. These have focused on deep convection, but more recently they have also addressed shallow convection (e.g., Deng et al. 2003; Bretherton et al. 2004). Such parameterizations make assumptions about the turbulent mixing of Cu clouds with the environment (Siebesma and Cuijpers 1995).

Entrainment mechanisms of Cu clouds have long been studied. Blyth (1993) describes Cu clouds as shedding thermals, with entrainment occurring near the ascending cloud-top and with mixed parcels descending around the edges of the thermal updraft core. This suggests that the source level of much of the diluted air measured at some level generally is at a higher level. The Large Eddy Simulation (LES) study by Heus et al. (2008) however shows that the Lagrangian tracking of air parcels reveals little cloud top entrainment: particle trajectories extracted from the LES runs clearly indicate that the main source of entrainment is lateral. Lateral entrainment yields characteristic horizontal variations of thermodynamic and moisture variables across the cloud edge. These characteristic variations have been documented by means of composite *in situ* data collected in a large number of aircraft penetrations through Cu and their immediate environment (Rodts et al. 2003; Wang et al. 2009; Wang and Geerts 2010).

Aside from lateral entrainment at any level, much entrainment also appears to result from a cloud-scale cloud-top vortex-ring (toroidal) circulation. Evidence for such circulation includes modeling simulations (Klaassen and Clark1985; Grabowski and Clark1993; Zhao and Austin 2005), observational studies using aircraft data (MacPherson and Isaac 1977; Blyth et al. 1988; Jonas 1990; Blyth et al. 2005), airborne radar data analyses (Damiani et al. 2006), trace gas analyses (Stith 1992) and tank experiments (Woodward 1959; Sanchez et al.1989; Johari1992). This toroidal circulation is important because it affects basic Cu characteristics, i.e. entrainment and detrainment, aerosol evolution, drop size distribution, hydrometeor recycling, and precipitation development. The toroidal motion can also dynamically affect the maximum height of Cu turrets, as the associated dynamic pressure deficit can oppose the suppressing effect of a dynamic pressure high resulting from the interaction between an updraft and the ambient vertical wind shear (Damiani and Vali 2007).

The radar observations by Damiani et al. (2006) and Damiani and Vali (2007) improved our understanding of vortex-ring circulations at cloud top, but they only showed the results from select case studies. The present study examines the generality of Cu cloud-top circulation patterns by compositing Doppler reflectivity and vertical velocity data from a large number of vertical transects collected in aircraft penetration of Cu clouds. The selection is unbiased as it includes all penetrations, between the Cu entry and exit points, subject only to a minimum cloud width and relative isolation from adjacent clouds. The objective is to show the characteristic reflectivity and vertical velocity structure in Cu, and stratify this as a function cloud age.

The data sources and analysis method are introduced in Section 2. The results are presented in Section 3, and their implications are discussed in Section 4. The main results are summarized in Section 5.

2. DATA SOURCES AND ANALYSIS METHOD

The Cu samples used in the present study were chosen from Cu clouds penetrated by the University of Wyoming King Air (WKA) in Arizona in summer as part of the 2006 Cu Photogrammetric, In-situ and Doppler Observations (CuPIDO) campaign (Damiani et al. 2008; Geerts et al. 2008). The detailed characteristics of sampled Cu will be discussed in Section 3.1.

2.1 Flight-level data

The WKA in-situ measurements have been discussed in many studies (e.g., Damiani et al. 2006;

* *Corresponding author address*: Yonggang Wang, Department of Atmospheric Science, University of Wyoming, Laramie, WY 82071, USA; email: wyg@uwyo.edu

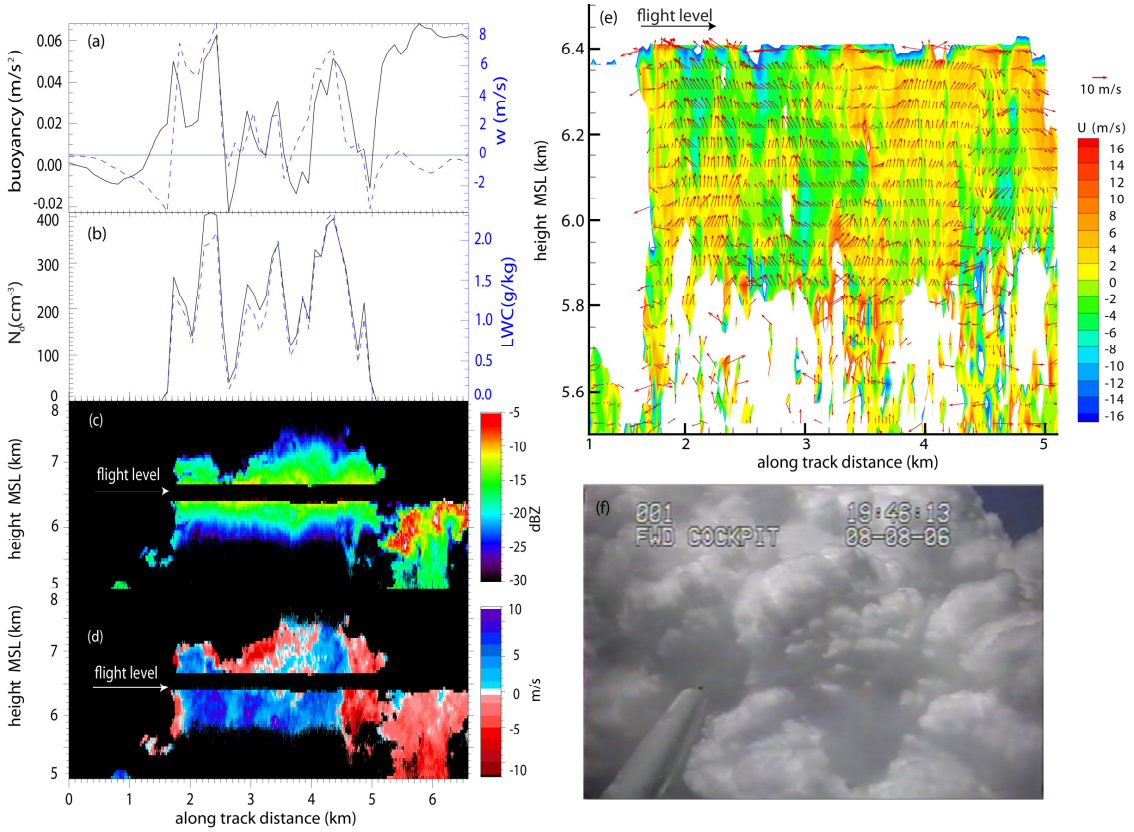

Fig. 1: Results of an up/down profiling scan of an isolated cumulus carried out at 1946 UTC 08 Aug 2006. Panel (a) shows flight-level buoyancy (solid line) and in situ measurements of gust probe vertical velocity (w, dashed line) collected at flight level (6.5 km MSL). Panel (b) shows in situ measurements of droplet concentration (N_d, solid line) and LWC (dashed line). Panels (c) and (d) show the WCR Doppler-retrieved reflectivity and vertical velocity. Panel (e) shows the VPDD analysis with the two-dimensional velocity field overlaid onto horizontal wind U (m/s). Panel (f) shows the Cu photo taken by a forward-pointing camera in the cockpit of the WKA at a time shown in the upper right corner.

Wang et al. 2009; Wang and Geerts 2011). Temperature is measured by a reverse flow thermometer which is an immersion probe developed to minimize in-cloud sensor wetting. The temperature has been corrected for the sensor evaporative cooling bias following Wang and Geerts (2009). The cloud liquid water content (LWC) and the cloud droplet concentration N_d (number of droplets per unit volume) are inferred from the Forward Scattering Spectrometer Probe (FSSP) (Brenguier et al. 1994). Vertical and horizontal air velocities are derived from the WKA gust probe (Lenschow et al. 1991). We inferred humidity variables from a chilled-mirror dewpoint sensor and assume in-cloud saturation and slowly varying conditions in the clear-air shell, as measured by the chilled-mirror dewpoint sensor for derived variables dependent on humidity, such as buoyancy.

2.2 Cloud radar data

The Wyoming Cloud Radar (WCR; Damiani et al. 2006) aboard the WKA is a 94 GHz (W-band), multiple-beam Doppler radar which operates mainly in two modes: up/down profiling mode and vertical-plane dual-Doppler (VPDD) mode (Fig. 1 in Damiani et al. 2006). The along-track two-dimension (2-D) air circulation below the aircraft can be derived if the WCR operates in the VPDD mode. The WCR profiling data are used for the composite analysis in this study: these data portray the vertical structure of an echo over its entire depth except for a 220-m-deep blind zone centered at flight level. The extraction of the echo's ground-relative motion from the Doppler velocity measured from a moving platform, and the dual-Doppler synthesis, are discussed in Leon et al. (2006) and Damiani and Haimov (2006). In a turbulent

environment such as a Cu cloud, the velocity uncertainty is about 1 m s^{-1} at ranges less than 2 km (Damiani and Haimov 2006).

The Cu clouds targeted in CuPIDO formed over the Santa Catalina Mountains in Arizona close to local solar noon, often before deep convection broke out. These clouds typically were rather shallow (~2 km deep), and had much liquid water (Wang et al. 2009). The WCR often lacked the sensitivity to detect the whole cloud. In fact the cloud base was usually not seen, as droplets near cloud base were too small, and the radar power was attenuated by water along the path. Sometimes the WCR could "see" below the sounding-derived cloud base, presumably because some rain drops fell below cloud base before evaporating. The emphasis will be on the upper part of the cloud, which generally was captured well by the WCR.

An example of the combined in-situ and vertical profile WCR data is shown in **Fig. 1**. Panel (a) shows in-situ measurements of gust probe vertical velocity and flight level buoyancy [1] and panel (b) shows measurements of droplet concentration and LWC collected at flight level. The flight-level droplet count indicates the width of the visible cloud along the track, in this case ~ 3 km. This Cu is characterized by positive buoyancy with rising motion at flight level. Panel (f) visually illustrates the target Cu. Panels (c) and (d) show the WCR reflectivity and Doppler-retrieved vertical velocity. The reflectivity is rather low with highest values (~-5 dBZ) near flight level.

The observed decrease in reflectivity with range is partly due to attenuation by liquid water: the power extinction coefficient at 94 GHz is 4.6 dB km^{-1} per g m^{-3} of cloud water, which includes the extinction by water vapor (Vali and Haimov 1999). In some areas flight-level liquid water content exceeds 1 g m^{-3} (Fig. 1b). Yet the decrease in reflectivity with range along the downward antenna in the target Cu cloud (about 20 dB km^{-1}) is almost an order of magnitude more rapid than expected from power extinction by liquid water alone, considering that the adiabatic liquid water content decreases with range (downward). So the rapid reflectivity increase towards flight level must be due in part to droplet growth. It should be noted that the quality of the Doppler velocity data is not affected by attenuation, as long as the signal remains above a range-dependent noise level. The lower half of the cloud is not detected by the WCR and lacks Doppler velocity data. A sounding released within 30 minutes and 30 km from this Cu cloud indicates that the ambient lifting condensation level (LCL, i.e. the cloud base) is 3900 m MSL, i.e. 1.5-1.9 km below the lowest level with WCR data in this cloud. The dual-Doppler synthesis of vertical and along-track winds (Fig. 1e) shows a single broad updrafts below flight level, flanked by more narrow downdrafts. The horizontal flow generally is weaker than the vertical flow. There is an updraft-downdraft dipole on the right (near 4.0<x<4.6 km), but there is little evidence for a closed circulation.

The vertical velocity shown in Fig. 1 and in the composite analyses below is the sum of the vertical air motion and the (downward) fall speed of the cloud particles. The reflectivity of the target clouds is rather low, with a maximum value of -10 dBZ on average. Most clouds in the composite entirely are composed of liquid water. None of the CuPIDO Cu penetrations contain measurable ice at flight level, but the increase in reflectivity aloft or in the post-mature stage suggests glaciation in some cases (as in the cloud on the right in Fig. 1c, which is not included in the composite because of lack of WCR echoes above flight level). In general it can be surmised that the particle diameter is small, and that the fall speed (or "terminal velocity"), although variable, probably is negligible compared to the convective up- and downdrafts such as those evident in sample Cu cloud shown in Fig. 1.

2.3 Analysis method

In order to composite cloud structure, the spatial dimensions of each cloud need to be normalized. Height in cloud (z) is normalized between cloud base and cloud top ($0<z^*<1$). The cloud top is defined as the highest echo seen by the WCR above the WKA during Cu penetration. Near-cloud-top echoes normally are strong enough, but our cloud top definition is an underestimate when the aircraft track is not right under the cloud top (e.g. for a tilted or cone-shaped Cu). As mentioned before, the cloud base cannot be seen by the WCR, so it is defined as the LCL, computed from potential temperature and mixing ratio data mixed in the lowest 50 hPa above the surface for all CuPIDO cases, using close-proximity GAUS (GPS Advanced Upper-air Sounding) data collected as part of the CuPIDO campaign.

We define the normalized distance $x^* \equiv 0$ at the cloud center and $x^* \equiv 1$ at the cloud edge. The cloud edge is not readily definable, as it varies with height. In the present study, the cloud width is defined as the distance between the two cloud edges seen by the WCR near flight level, and the cloud center is defined as the location with the distance to either edge equal to half of the cloud width. This width has to be at least 400 m. Cases thus defined with a separation of less than 400 m were excluded as well, because those

[1] Cloud buoyancy is computed from temperature, humidity, and cloud liquid water following equation 2.79 in Markowski and Richardson (2010). Pressure perturbations are ignored. The basic state variables in the buoyancy equation are computed over a distance of 0.5 km in the clear air adjacent to the cloud.

clouds usually were part of a single cloud below flight level.

The CuPIDO dataset yields a total of 260 good half-clouds. The WCR reflectivity field[2] and vertical velocity field then are averaged in a 2-D (the along-track coordinate x^* and the altitude coordinate z^*) frame centered in the Cu core ($x^* = 0$) and at cloud base ($z^* = 0$), with a bin size $\Delta x^* = 0.02$ and $\Delta z^* = 0.02$. The WCR horizontal and vertical resolution is 9x30 m (nadir) to 14x30 m (zenith) at a typical range of 1 km in CuPIDO. The bin size (Δx^*, Δz^*) is selected as a trade-off between limiting the smoothening of the largest clouds and resolution redundancy for the smallest clouds. For instance, for the cloud shown in Fig. 1, the width is 3 km, the depth 3 km, thus (Δx^*, Δz^*) corresponds with (60, 60) m. This implies smoothening mainly in the horizontal ($\Delta x^* >> 14$ m), and less in the vertical ($\Delta z^* > 30$ m). In rather large/deep cloud, this data redistribution process results in less-defined cloud edges and the smoothening of extreme values.

were collected over the Santa Catalina Range. This is a rather isolated mountain with almost daily Cu development during the monsoon period. The data were collected before and around local solar noon; on most days, deep convection ensued later in the afternoon, although the transition from shallow to deep convection often is a very gradual process (Zehnder et al. 2006).

The sampled CuPIDO Cu clouds occurred in an environment with low-level potential instability, up to ~4.7 km MSL or ~2.0 km above the Santa Catalina Range. A rapid transition to a potentially stable environment occurs at 4.7 km MSL (Fig. 2a). With a cloud base around 3.0 km MSL (Fig. 2b), this yields a good environment for lightning-free Cu development. The mean level of free convection (LFC) is at about 3.5 km MSL (Fig. 2a). The CAPE values for the 16 CuPIDO soundings used ranged between 32 and 2547 J kg^{-1}, with an average value of 1044 J kg^{-1}.

The sampled cumuli in CuPIDO were generally of the *humilis* to *mediocris* type. Cloud depths ranged

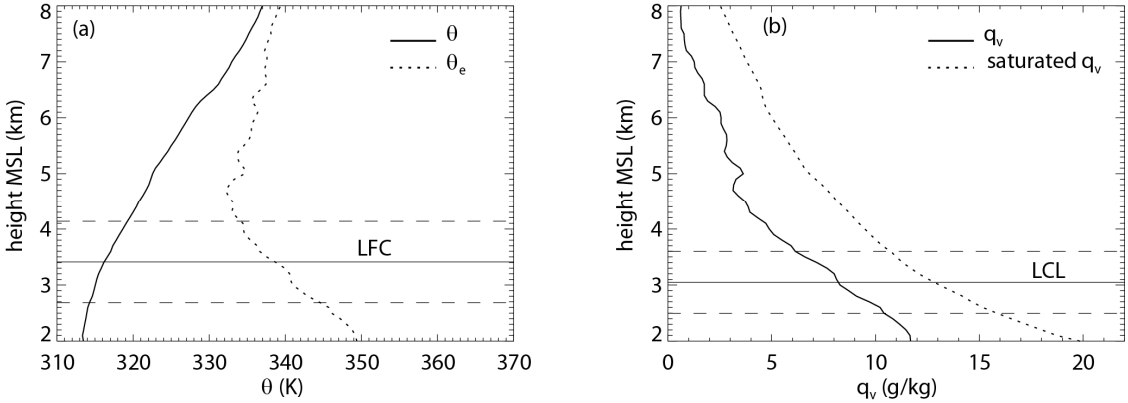

Fig. 2: (a) Typical profile of potential temperature (θ) and equivalent potential temperature (θ_e), obtained from 16 M-GAUS sondes released at Windy Point on the south flank of the Santa Catalina Range in Arizona during WKA flights between 2006/07/24 and 2006/08/17; the horizontal lines are the mean LFC and LFC ± 1 standard deviation. (b) As (a), but for specific humidity (q_v) and saturated specific humidity; the horizontal lines are the mean LCL and LCL ± 1 standard deviation.

3. Composite structure of shallow Cu

3.1 Basic characteristics of the sampled Cu clouds and their environment

The typical environment of the Cu clouds penetrated during CuPIDO is inferred from proximity Mobile GAUS (M-GAUS) radiosonde data (**Fig. 2)**. These radiosondes were released in close proximity of the target Cu clouds, all within 50 km and 1 hour of the flight data. The CuPIDO sounding and flight data

from a few 100 m to ~4000 m, with a most common estimated depth of 1900 m (**Fig. 3**b). Some 62% of the penetrated Cu was less than 2 km wide, yet some Cu were just over 4 km wide. Flight-level temperatures ranged from -8 to +12°C (Fig. 3c), and most CuPIDO clouds contained ice. The updrafts were as strong as 15 m s^{-1}, according to WCR data, but some 80% of the clouds had peak updrafts between 3-10 m s^{-1}. We also computed the cloud-average air (gust probe) vertical velocity at flight level for the sampled Cu (Fig. 3e). There was a range of vertical velocities in the sampled Cu, implying that all stages in the lifecycle of Cu towers were sampled. While the majority of clouds had rising motion, a

[2] The radar reflectivity is averaged in units of Z (mm^6 m^{-3}). The average Z then is reconverted to dBZ units.

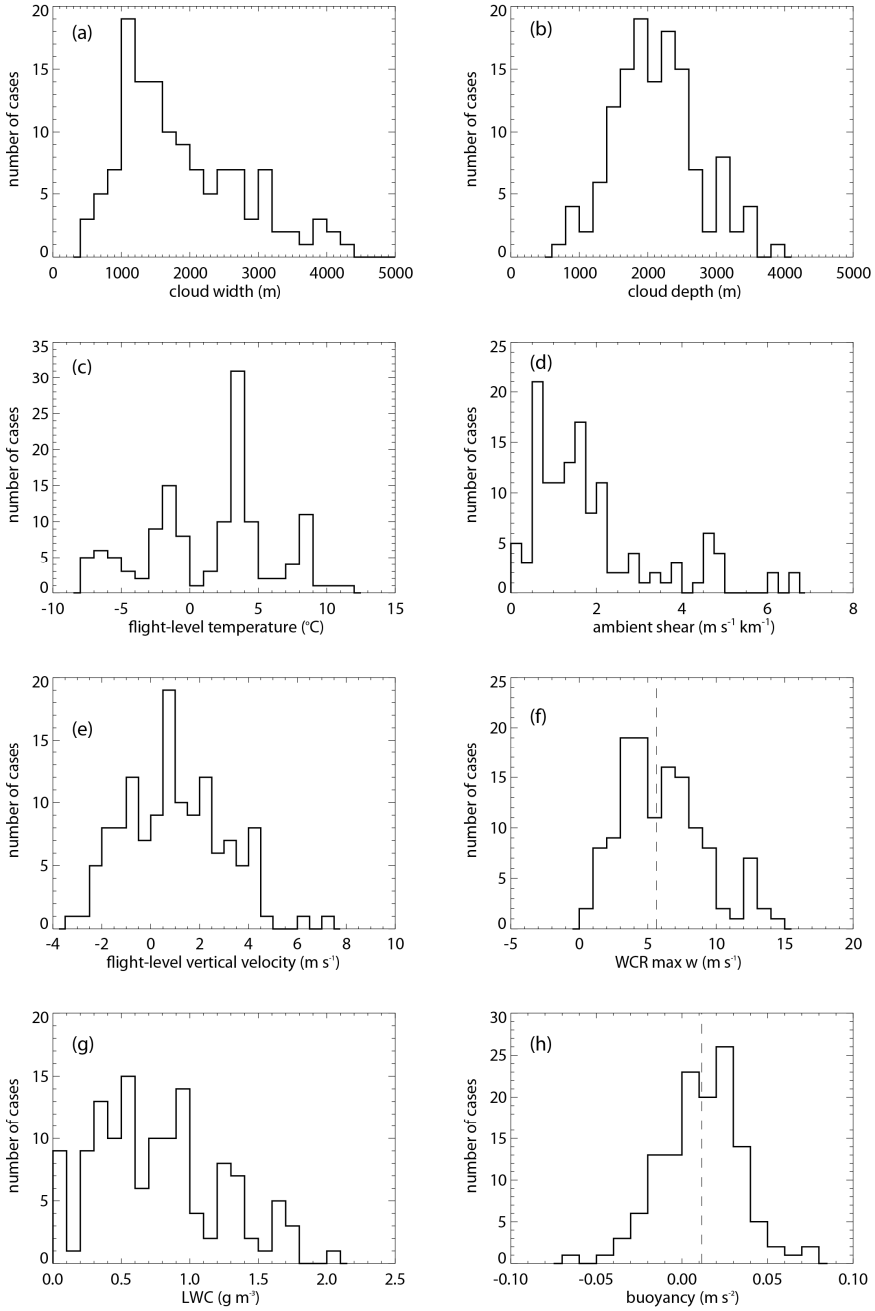

Fig. 3: Histograms of the mean properties of the 130 cumuli in CuPIDO: (a) cloud width; (b) cloud depth; (c) flight-level temperature; (d) ambient shear; (e) flight-level vertical velocity; (f) WCR maximum vertical velocity; (g) LWC; (h) flight level buoyancy. The dashed lines in panels (f) and (h) show the modus values to stratify subsets.

significant fraction of the Cu was sampled in their decaying phase with mainly sinking motion at flight level. Just over 30% of the Cu clouds were negatively buoyant. Negatively buoyant, sinking Cu may have been oversampled, simply because of the time lag between targeting and penetrating a candidate cloud, but we can stratify the composite results by means of cloud buoyancy or vertical velocity.

In short, the dataset of 130 Cu penetrations represents mostly relatively shallow, non-precipitating Cu in a range of dimensions, Cu lifecycle stages, and ambient conditions.

3.2 Composite reflectivity and vertical velocity

Fig. 4 shows the composite reflectivity and vertical velocity for 260 half-clouds from CuPIDO while the WCR operated in profiling mode. The data frequency distribution (Fig. 4c) confirms that at least the lowest 20% of the Cu clouds could not be detected by the WCR, in part because of the weak echo expected from small droplets near cloud base, but also due to attenuation, since the WKA mostly flew in the upper half of the clouds during CuPIDO (black curve in Fig. 4c). To reduce the statistical uncertainty caused by a small sample size, we only show composite data where the absolute frequency is larger than 20.

The radar echoes are generally quite weak with the average reflectivity in the range from -24 to -8 dBZ (Fig. 4a). The reflectivity in upper part with high frequency (h^* ~ [0.4, 1]) is generally more uniform within Cu than the region close to Cu edge and the radar echoes are stronger within Cu. This may imply that lateral entrainment of dry environment air occurs at the region close to Cu edge. Since the measurement of reflectivity is a combination of droplet concentration and droplet size, this is consistent with the finding of Wang et al. (2009) using WKA flight level measurements: the droplet concentration and the mean droplet size generally decrease in value from within the Cu towards the cloud edge due to entrainment and detrainment. The weak echoes at radar-sensed cloud upper boundary (h^* ~ 1.0) identify the mixture of cloudy and ambient air and can act as the evidence of cloud-top entrainment.

Two things need to be noted in the composite of radar vertical velocity (Fig. 4b). Firstly, sinking motion dominates the lower part of Cu with h^* ranging from 0.2 to 0.55, while the air vertical motion transits from rising motion to sinking motion at the region with h^* above 0.55 and the transition at cloud-top is found at x^* approximately equals to 0.5. Secondly, strong buoyantly driven subsidence is observed at cloud edge, which provides further evidence for significant evaporative cooling in laterally entraining and detraining eddies in the cloud margin, which is defined as a transition zone within ~10% of the cloud diameter of the cloud edge in Wang et al. (2009).

The WCR composite analysis shows clear evidence of the existence of a vortex-ring circulation. Firstly, the radar vertical velocity field shows that an updraft/downdraft dipole is observed near cloud top with updraft close to cloud center and downdraft close to cloud edge, consistent with the observation from

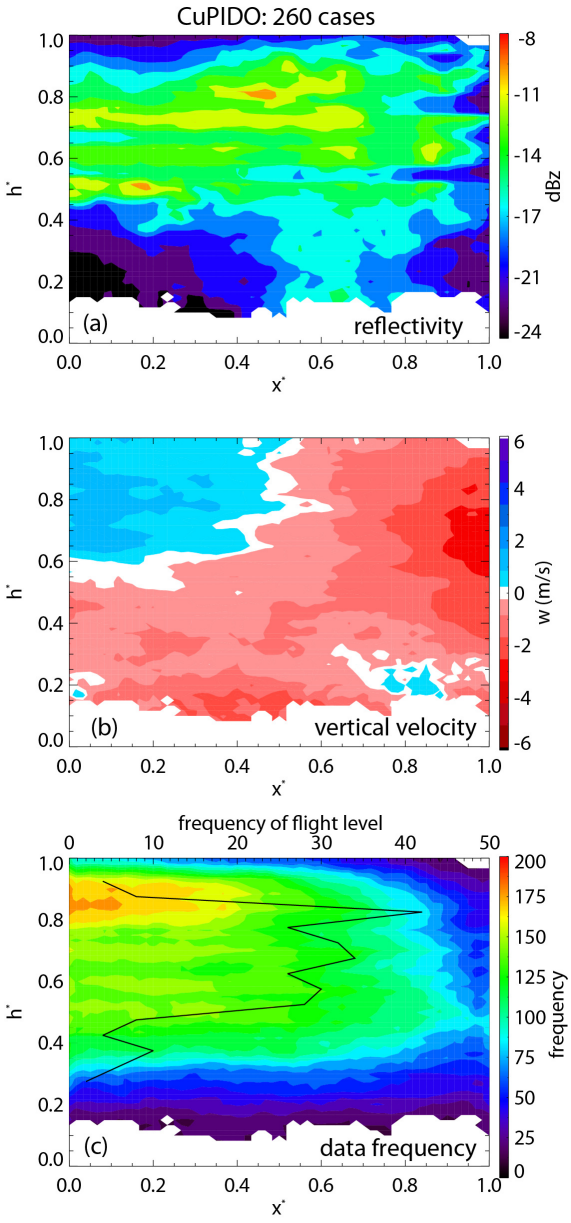

Fig. 4: Variation of WCR Doppler-retrieved variables with normalized distance from the cloud center (x^*= 0) to the cloud edge (x^*= 1) and normalized height from the cloud base (h^*= 0) to the cloud top (h^*= 1): (a) reflectivity, (b) vertical velocity, (c) data frequency and the black line is the frequency of WKA flight levels. The number of cases is listed on top of plot.

case studies. Secondly, the strong radar echoes are found at the Cu upper part (h^* ~ [0.6, 0.9]) and at the center between Cu core and Cu edge (x^* ~ [0.3, 0.7]),

which is in accordance with the transition zone from rising motion to sinking motion in radar vertical velocity field, suggesting that the swirling motion has captured large hydrometeors at Cu center and driven these hydrometeors upward and farther away from Cu center. Thirdly, Cu are more inhomogeneous in terms of both reflectivity field and vertical velocity field near their buoyant top and more homogenous in the lower cloud region marked by smaller buoyancy and weaker updrafts. The maximum updraft speed occurs at the upper part of Cu close to Cu center indicating that this is the center of the vortex-ring.

3.3 The effect of Cu life cycle stage on the cloud-top vortex-ring

To study the effect of Cu life cycle stages on the circulation pattern, we stratified all the Cu into strongly-rising/weakly rising (or sinking) and more/less buoyant subgroups because statistically speaking the developing young Cu tend to be positively buoyant with rising motion while sinking motion is generally associated with decaying Cu which are negatively buoyant.

Fig. 5a and b **and Fig. 6a** and b compare the composite results for the subsets of Cu with strongly-rising and weakly-rising motions. The maximum WCR vertical velocity for each case has been used to do the stratification with the threshold maximum WCR updraft speed as 5.6 m s^{-1}, shown as the dashed line in Fig. 3f. The updraft/downdraft dipole only exists in the subgroup with stronger rising motion, but not in the subgroup with weak rising/sinking motion, suggesting that the vortex-ring circulation occurs more often in young Cu than in decaying Cu. By comparing Fig. 4b and Fig. 5a, we can see that the updraft/downdraft dipole has extended vertically from the upper part of Cu (h^* ~ [0.55-1.0]) in the average of all Cu to a deeper region (h^* ~ [0.3-1.0]) in the subset of Cu cases with strong rising motion. This observation is meaningful for cloud entrainment: it is an indication that entrainment of ambient air occurs more often in developing Cu than decaying Cu, since the cloud-free air is drawn into the rising thermal at the bottom of the vortex-ring (Blyth 1988; Carpenter et al. 1998; Damiani et al. 2006). Another thing to notice is that the transition zone between the updraft and downdraft regions has moved towards the Cu edge in the subgroup with strong upward motion compared with the average of all Cu.

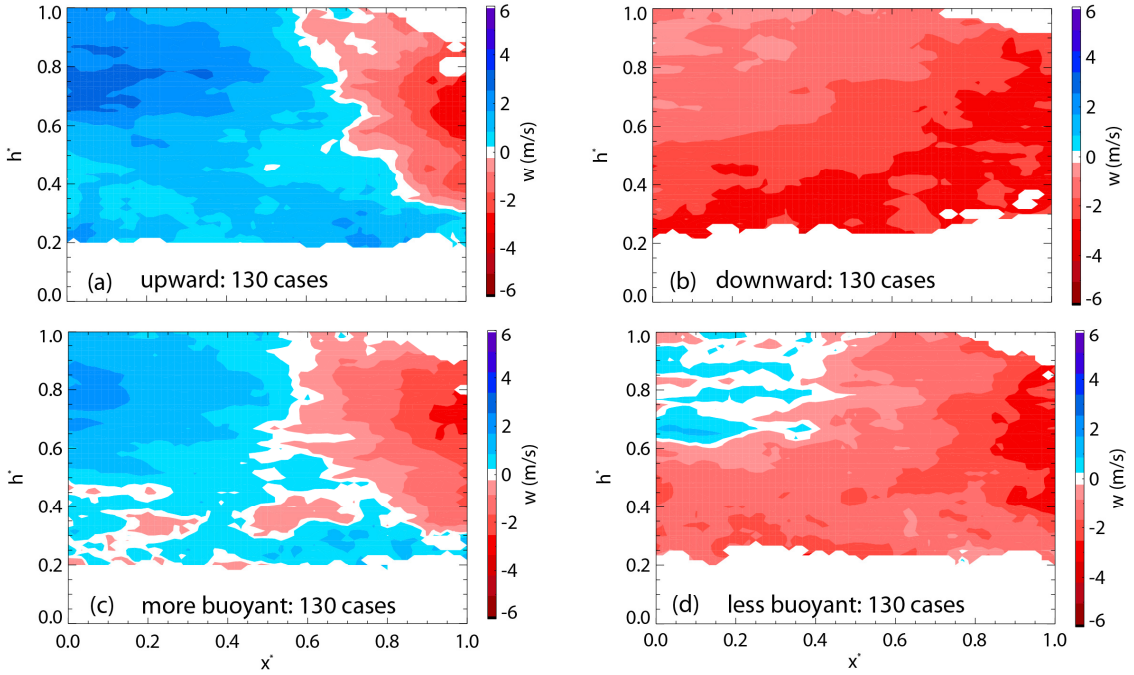

Fig. 5: Variation of WCR Doppler-retrieved vertical velocity with normalized distance from the cloud center (x^*= 0) to the cloud edge (x^*= 1) and normalized height from the cloud base (h^*= 0) to the cloud top (h^*= 1) for different subsets. (a) Strongly-rising Cu and (b) weakly-rising or sinking Cu. The threshold vertical velocity that partitions the total population in two equal parts (the modus) is 5.64 m s^{-1}. (c) More buoyant Cu and (d) less buoyant Cu. The modus cloud-mean buoyancy is 0.012 m s^{-2}.

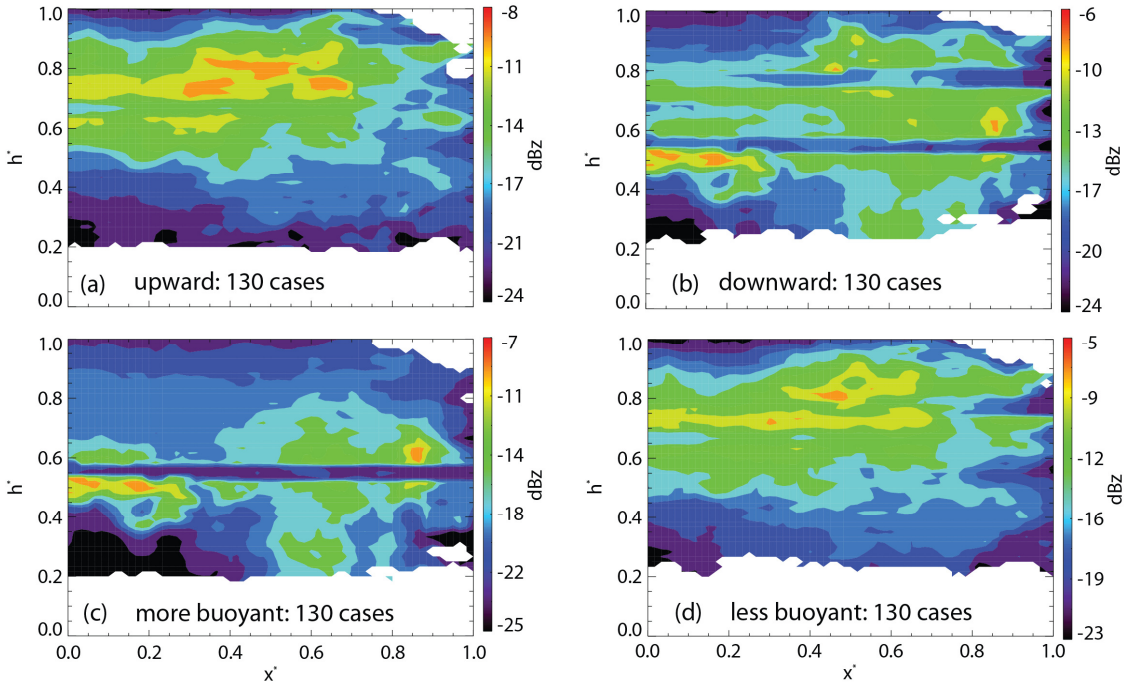

Fig. 6: As Fig. 5, but for WCR Doppler-retrieved reflectivity.

Fig. 5c and d and Fig. 6c and d show the comparison between the more and less buoyant Cu. The calculation of buoyancy B (m s^{-2}) is introduced in Section 3.1 and the in-cloud value of q_v is assumed to be the saturated value computed from local temperature and pressure, while the measurement from the chilled-mirror dewpoint sensor is used for q_v outside of cloud.

It can be observed from Fig. 5c and d that the updraft/downdraft dipole exists in both subgroups. However, the region of ascending air is wider and deeper for the more buoyant subgroup than the less buoyant subgroup. Combining this observation with what have been observed for Cu with strong-rising and weakly-rising motions, we can say that the vortex-ring circulation is initiated in young Cu that are more buoyant with strongly-rising motion and tends to move to Cu tops as Cu develop and decays in less buoyant Cu with weakly-rising or sinking motion.

4. DISCUSSION

The Doppler vertical velocity field of individual Cu clouds shows that vortex-ring structure is complex and multi-vortex structure is commonly observed (Fig. 1; Damiani et al. 2006). However, single-ring-vortex entrainment patterns have been observed in the composite analysis of 260 half-cloud in the present study. The scale of the single-ring-vortex structure is comparable to the scale of Cu, both in depth and in width. This indicates that vortex-ring structure may dominate the entrainment process at Cu top, at least in the developing stage of Cu. The observation of cloud-scale vortex-ring structures is significant because they are thought to be key players in the entrainment mechanisms. In particular, a cloud-scale toroidal circulation reduces the buoyancy more effectively than laterally-mixing eddies, because the typical lateral mixing length is only 10-15% of the cloud diameter (Wang et al. 2009; Wang and Geerts 2010).

The result also illustrate the potential of the composite technique for future studies of Cu. Due to the complex structure, transient nature and great inhomogeneity of Cu, individual case studies of Cu have a high degree of limitation. The successful application of composite technique in this observational study provides confidence to future studies of Cu in model simulations. This study composites only single-Doppler fields derived from cloud radar, but it is expected that the composite of dual-Doppler fields of many Cu will provide more details about Cu circulation patterns. In the present study, dual-Doppler composite is not pursued because dual-Doppler (u, w) synthesis is possible only below flight level, and thus, to capture the toroidal circulation, the aircraft has to fly above cloud top, yielding no cloud in situ information at all.

5. CONCLUSIONS

This observational study is the first one to examine typical circulation patterns of shallow cumulus clouds by compositing the reflectivity and Doppler vertical velocity data from an airborne mm-wave cloud radar for many Cu clouds in various stages of their life cycle. The following results have been reached:

- The composite analysis proves the existence a horizontal vortex-ring largely contained within cloud by showing clear evidence of an updraft/downdraft dipole near cloud top.
- This single-ring-vortex picture emerges notwithstanding the complex multi-vortex structure commonly evident in individual transects of Cu clouds.
- The vortex-ring circulation patterns tend to be more common and more intense in positively buoyant Cu with rising motion than negatively buoyant and/or sinking Cu near the end of their life cycle.

Acknowledgements: This work was supported by National Science Foundation (NSF) grants ATM-0444254 and ATM-0849225. We thank the crew of the University of Wyoming King Air for collecting the data and providing high-quality products for the CuPIDO campaign.

References

Blyth, A. M., 1993: Entrainment in cumulus clouds. *J. Appl. Meteor.*, **32**, 626–641.

Blyth, A. M., W. A. Cooper, and J. B. Jensen, 1988: A study of the source of entrained air in Montana cumuli. *J. Atmos. Sci.*, **45**, 3944–3964.

Blyth, A.M., S. G. Lasher-Trapp, and W. A. Cooper, 2005: A study of thermals in cumulus clouds. *Quart. J. Roy. Meteor. Soc.,* **131**, 1171–1190.

Brenguier, J., D. Baumgardner, and B. Baker, 1994: A review and discussion of processing algorithms for FSSP concentration measurements. *J. Atmos. Ocean. Tech.*, **11**, 1409–1414.

Bretherton, C. S., J. R. McCaa, and H. Grenier, 2004: A new parameterization for shallow cumulus convection and its application to marine subtropical cloud-topped boundary layers. Part I: Description and 1D results. Mon. Wea. Rev., 132, 864–882.

Carpenter, R.L., K.K. Droegemeier, and A.M. Blyth, 1998: Entrainment and Detrainment in Numerically Simulated Cumulus Congestus Clouds. Part III: Parcel Analysis. *J. Atmos. Sci.*, **55**, 3440–3455.

Damiani, R., G. Vali, and S. Haimov, 2006: The structure of thermals in cumulus from airborne dual-Doppler radar observations. *J. Atmos. Sci.*, **64**, 2045–2060.

Damiani, R., and G. Vali, 2007: Evidence for tilted toroidal circulations in cumulus. *J. Atmos. Sci.*, **63**, 1432–1450.

Damiani, R., J. Zehnder, B. Geerts, J. Demko, S. Haimov, J. Petti, G.S. Poulos, A. Razdan, J. Hu, M. Leuthold, and J. French, 2008: Cumulus Photogrammetric, In-situ and Doppler Observations: the CuPIDO 2006 experiment. *Bull. Amer. Meteor. Soc.,* **89**, 57–73.

Damiani, R., and S. Haimov, 2006: A high-resolution dual-Doppler technique for fixed multi-antenna airborne radar. *IEEE Trans. Geosci. Remote Sens.,* **42**, 3475–3489.

Deng, A., N. L. Seaman, and J. S. Kain. 2003: A shallow-convection parameterization for mesoscale models. Part I: Submodel description and preliminary applications. *J. Atmos. Sci.*, **60**, 34–56.

Geerts, B., Q. Miao, and J.C. Demko, 2008: Pressure perturbations and upslope flow over a heated, isolated mountain. *Mon. Wea. Rev.*, **136**, 4272–4288.

Grabowski, W. W., and T. L. Clark, 1993: Cloud-environment interface instability, Part II: Extension to three spatial dimensions. *J. Atmos. Sci.*, **50**, 555-573.

Heus, T., G. van Dijk, H.J.J. Jonker, and H.E.A. Van den Akker, 2008: Mixing in shallow cumulus clouds studied by Lagrangian particle tracking. *J. Atmos. Sci.*, **65**, 2581–2597.

Johari, H., 1992: Mixing in thermals with and without buoyancy reversal. *J. Atmos. Sci.,* **49**, 1412–1426

Jonas, P. R., 1990: Observations of cumulus cloud entrainment. *Atmos. Res.*, **25**, 105–127.

Khairoutdinov, M., C. DeMott, and D. Randall, 2008: Evaluation of the simulated interannual and subseasonal variability in an AMIP-Style simulation using the CSU Multiscale Modeling Framework. *J. Climate*, **21**, 413–431.

Klaassen, G.P., and T. L. Clark, 1985: Dynamics of the cloud-environment interface and entrainment in small cumuli: Two-dimensional simulations in the absence of ambient shear. *J. Atmos. Sci.*, **42**, 2621–2642.

Lenschow, D., E. Miller, and R. Friesen, 1991: A three-aircraft intercomparison of two types of air motion measurement systems. *J. Atmos. Ocean. Tech.*, **8**, 41–50.

Leon, D., G. Vali, and M. Lothon, 2006: Dual-Doppler analysis in a single plane from an airborne platform. *J. Atmos. Ocean. Tech.*, **23**, 3-22.

Lopez, R. E., 1977: The lognormal distribution and cumulus cloud populations. *Mon. Wea. Rev.*, **105**, 865–872.

MacPherson, J. I., and G. A. Isaac, 1977: Turbulent characteristics of some Canadian cumulus clouds. *J. Appl. Meteor.,* **16**, 81– 90.

Markowski, P., and Y. Richardson, 2010: Mesoscale Meteorology in Midlatitudes. *John Wiley & Sons, Ltd, Chichester, UK.*, doi: 10.1002/9780470682104..

Rodts, S.M.A., P.G. Duynkerke, and H.J.J. Jonker, 2003: Size distributions and dynamical properties of shallow cumulus clouds from aircraft observations and satellite data. *J. Atmos. Sci.*, **60**, 1895–1912.

Sanchez, O., D. Raymond, L. Libersky, and A. Petschek, 1989: The development of thermals from rest. *J. Atmos. Sci.,* **46**, 2708–2718.

Siebesma, A. P. and J. W. M. Cuijpers. 1995. Evaluation of parametric assumptions for shallow convection. *J. Atmos. Sci.*, **52**, 650–656.

Stith, J. L.,1992: Observations of cloud-top entrainment in cumuli. *J. Atmos. Sci.,* **49**, 1334–1347.

Vali, G. and S. Haimov, 1999: Observed extinction by clouds at 95 GHz. *IEEE Trans. Geosc. Rem. Sens.*, **39**, 190-193.

Wang, Y., and B. Geerts, 2010: Humidity variations across the edge of trade wind cumuli: observations and dynamical implications. *Atmos. Res.*, **97**, 144-156. doi:10.1016/j.atmosres.2010.03.017.

Wang, Y., and B. Geerts, 2009: Estimating the evaporative cooling bias of an airborne reverse flow thermometer. *J. Atmos. Ocean. Tech.*, **26**, 3-21.

Wang, Y., B. Geerts, and J. French, 2009: Dynamics of the cumulus cloud margin: an observational study. *J. Atmos. Sci.*, **66**, 3660-3677.

Wang, Y., and B. Geerts, 2011: Observations of detrainment signatures from non-precipitating orographic cumulus clouds. *Atmos. Res.,* 99, 302-324.

Wielicki B. A., and R. M. Welch, 1986: Cumulus cloud properties derived using Landsat satellite data. *J. Climate Appl. Meteor.*, **25**, 261–276.

Woodward, B., 1959: The motion in and around isolated thermals. *Quart. J. Roy. Meteor. Soc.*, **85**, 144–151.

Zehnder, J. A., L. Zhang, D. Hansford, A. Radzan, N. Selover, and C. M. Brown, 2006: Using digital cloud photogrammetry to characterize the onset and transition from shallow to deep convection over orography. *Mon. Wea. Rev.*, **134**, 2527–2546.

Zhao, M., and P.H. Austin, 2005: Life Cycle of numerically simulated shallow cumulus clouds. Part II: Mixing dynamics. *J. Atmos. Sci.*, **62**, 1291–1310.